On the Misclassification of Dust as Cloud at an AERONET site in the Sonoran Desert

Amato Evan*, Blake Walkowiak, Robert Frouin

Scripps Institution of Oceanography, University of California San Diego

**Corresponding author address:* Amato Evan, Scripps Institution of Oceanography, University of California San Diego, La Jolla, CA 92104

E-mail: aevan@ucsd.edu

ABSTRACT

Here we present retrievals of aerosol optical depth τ from an Aerosol Robotic Network (AERONET) station in the southeastern corner of California, an area where dust storms are frequent. By combining AERONET data with collocated ceilometer measurements, camera imagery, and satellite data, we show that during significant dust outbreaks the AERONET cloud-screening algorithm oftentimes classifies dusty measurements as cloud contaminated, thus removing them from the aerosol record. During dust storms we estimate that approximately 85% of all dusty retrievals of τ and more than 95% of retrievals when $\tau > 0.1$ are rejected, resulting in a factor 2 reduction in dust-storm averaged τ. We document the specific components in the screening algorithm responsible for the misclassification. We find that a major reason for the loss of these dusty measurements is the high temporal variability in τ during the passage of dust storms over the site, which itself is related to the proximity of the site to the locations of emission. We describe a method to recover these dusty measurements that is based on collocated ceilometer measurements. These results suggest that AERONET sites located close to dust source regions may require ancillary measurements in order to aid in the identification of dust.

SIGNIFICANCE STATEMENT: In this study we demonstrate that during dust storms, measurements made with a sun photometer at an AERONET site in the Western Sonoran Desert are frequently classified as cloud contaminated by the network's processing algorithm. We identify the various algorithmic tests that result in the misclassification and discuss the physical reasons why dust typically fails those tests. We then present a method to restore these data that utilizes measurements from a collocated ceilometer. This work highlights the challenges, and one solution, to operating an AERONET site in a region that is close to the sources of airborne dust.

1. Introduction

By mass, aeolian dust is the most abundant aerosol in the Earth's atmosphere (Kok et al. 2017) and affects the global energy budget directly via absorption and scattering of radiation (Mahowald et al. 2010; Miller and Tegen 1998; Myhre and Stordal 2001). Dust is also observed to be an ice nucleating particle (Ansmann et al. 2008), and thus may impact the global climate via the glaciation effect (DeMott et al. 2010). Furthermore, long-range dust transport and subsequent deposition is thought to be an important source of nutrients to remote ocean and terrestrial ecosystems (Das et al. 2013; Okin et al. 2011), which can in-turn alter the global carbon cycle (Mahowald et al. 2010).

Although the processes by which dust directly and indirectly affects the global climate have been described, quantifying their respective magnitudes is challenging. For example, there is such wide disparity in estimates of the direct radiative effect that the sign of the globally averaged forcing is not known (Kok et al. 2017), and model estimates of the global dust burden vary by an order of magnitude (Huneeus et al. 2011). Certainly one cause of the uncertainty in understanding the nature of dust in the Earth's climate system is a relative paucity of observational data, which stems from the fact that most dust storms originate in sparsely populated regions (Prospero et al. 2002).

Probably the most ubiquitous and widely-used record of dust is from the AEROsol RObotic NETwork (Holben et al. 1998, AERONET). AERONET is a global network of sun photometers making direct solar irradiance measurements that are used to retrieve aerosol optical depth τ at different wavelengths. Although τ is a measure of the vertically integrated extinction of light by an aerosol, it is also directly proportional to the column integrated aerosol mass. As such, retrievals of τ from AERONET stations impacted by dust are widely used by the research community, especially given the accuracy of the retrievals (Dubovik et al. 2000). For example, AERONET data has long been used to evaluate the representation of dust in climate models (Huneeus et al. 2011; Albani et al. 2014), validate dust products from satellite data (Zhou et al. 2020; Habib et al. 2019; Peyridieu et al. 2013), estimate dust occurrence frequency (Toledano et al. 2007), and characterize dust optical properties (Kim et al. 2011).

Here we present measurements from a new AERONET station located on the western edge of the Sonoran Desert, a region where dust storms frequently occur (Evan 2019). Specifically we report how a processing algorithm for AERONET retrievals of τ, which is intended to screen the data for artifacts and cloud contamination, regularly rejects measurements made during dust storms as cloud contaminated. We find that several of the spectral and temporal variability-based tests are not effective at separating dust from clouds, at least at this one site. The purpose of this document is to serve as a reference for users of the data from this site and for other potential AERONET sites situated closely to dust source regions.

The paper is organized as follows. In Section 2 we describe the field site, instrumentation, and measurements utilized in this study. In Section 3 we examine measurements made during a dust outbreak on January 29, 2020, and identify the specific components of the AERONET processing algorithm that result in the rejection of dusty measurements as cloud-contaminated. In Section 4 we broaden our findings and examine measurements made during dust storms on 12 separate days. Finally, in Section 5 we summarize our findings and conclude on potential implications of screening out dusty measurements on the AERONET aerosol record.

2. Field site and data

The Salton Sea AERONET field site is located at 33.17°N and -115.86°E (blue square, Fig. 1). This sub-sea level site is at an elevation of -32 m above mean sea level, lies directly to the east of the Anza Desert, and is approximately 2.5 km from the shoreline of the Salton Sea. As such, the site is well positioned to measure dust emitted both from desert and dry playa sources. The landscape immediately surrounding this site includes dirt roads, citrus and date palm orchards, and barren shrublands.

The AERONET instrument at this site is a CIMEL Electronique Sun–sky photometer, which is used to measure Sun collimated direct beam irradiance and directional sky radiance at 8 spectral bands centered on 1020, 870, 675, 440, 936, 500, 380, and 340 nm (Holben et al. 1998). The instrument base is mounted approximately 2 m above the ground level. Direct solar irradiance measurements are made at 5-minute intervals and directional radiances in the almucantar and principle planes are made at 30-minute intervals. The data are inverted in order to determine aerosol properties in the total atmospheric column via algorithms described in (Dubovik and King 2000) and (Dubovik et al. 2000).

Here we utilize data from the AERONET Level 1.0 (hereafter L1) and Level 1.5 (hereafter L1.5) products. The L1.5 AERONET products are processed by the Version 3 AERONET algorithm (hereafter referred to as the V3 algorithm), which provides fully automatic cloud screening and instrument anomaly quality controls in near-real-time (Giles et al. 2019). Thus, optical depth τ from the L1 products may be contaminated by clouds, whereas τ from the L1.5 products is only reported for clear-sky conditions. The V3 algorithm tests that are most relevant to this study are summarized in Table 1.

Also located at this site is a Vaisala CL51 ceilometer, which is a single lens lidar system that makes continuous profiles of attenuated backscatter BS at a nominal wavelength of 910 nm and up to heights of 15 km. The CL51 range corrected BS profiles used here are generated at a 36 s temporal resolution and a 10 m vertical resolution. In addition to cloud detection, ceilometers, including the CL51, have shown to be useful in the detection of aerosol layers in the lower troposphere (Münkel et al. 2007; Wiegner et al. 2014; Jin et al. 2015; Marcos et al. 2018; Yang et al. 2020). The Vaisala processing software for the CL51 measurements (BLView) produces retrievals of vertical profiles of extinction σ and optical depth τ from the BS profiles for the clear-sky atmosphere below 5 km. Although details regarding the retrieval process used in BLView are not publicly available, we were able to produce extinction profiles that were qualitatively similar to those from the BLView software using the methods described in Fernald (1984), suggesting that BLView uses a similar method to retrieve extinction profiles and calculate aerosol optical depth (we note that the differences between our retrievals of extinction and those from BLView appeared to be associated with a smoothing procedure applied to the range corrected signal prior to application of the retrieval algorithm, and a scaling factor difference between the two).

We utilize hourly-averaged measurements of 10 m wind speed and direction and 10 μm particulate matter concentrations PM_{10} made at a number of sites around the Salton Sea. We also present images from a 360° Roundshot web camera that is located approximately 28 km west of the field site at an elevation of just over 300 m (red square, Fig 1). Roundshot images are available at approximately 10 min intervals during daytime hours.

Lastly, we incorporate into our analysis satellite imagery from the Moderate Resolution Imaging Spectrometer (MODIS) flying onboard the Terra satellite, and from the Advanced Baseline Imager (ABI) flying onboard GOES-17.

3. Results

We begin with a case study of a dust outbreak that occurred on January 29, 2020. Based on surface and upper level charts from the National Oceanographic and Atmospheric Administration Weather Prediction Center and the Area Forecast Discussion from the San Diego National Weather Service field office, during the daytime hours of January 29, 2020 strong northerly low-level flow was prevalent across southern California due to an intensifying upper level low located to the east, and a building high pressure to the north (not shown). Hourly averaged wind speeds at the AERONET site peaked on this day at 11.4 m s^{-1} and at 330° at 20:00 UTC (not shown).

The northerly high winds on January 29 resulted in dust emission throughout the area. A true color image acquired at approximately 19:10 UTC from the MODIS instrument flying onboard the Terra satellite shows a northwest to southeast oriented plume of dust clearly visible over the western half of the Salton Sea (Fig. 1). A GOES-17 animation from 18:00 to 20:30 UTC shows dust being advected southeastward from the northern tip of the Salton Sea and over the field site (Supplemental Data). The presence of dust is also confirmed in imagery from the Roundshot camera (Fig. 1, red square) at 19:10 UTC, which shows dust in the westward direction and thus over the AERONET site (Fig. 2a). Also confirming the presense of dust are hourly averaged PM_{10} measurements from a location approximately 15 km NNW of our site (Salton City) peaked at 2000 μg cm^{-3} at 20:00 UTC on this day (not shown).

Backscatter profiles from the CL51 show a strong signal from the surface to heights of approximately 1.5 km AGL, starting at 18:30 UTC and terminating less than two-hours later at 20:20

UTC (Fig. 2b). At approximately 19:00 UTC the GOES=17 animation shows the dust plume orientation turning clockwise, which results in dust being advected directly over the AERONET site (Supplemental Data), and at this same time the magnitude of the *BS* signal also increases (Fig. 2b). At 19:00 there is also an apparent increase in the opacity of the dust in the GOES-17 animation, which implies that after this time a particularly dense component of the dust plume is over the site.

Having demonstrated that there was a dust storm in this region on January 29, 2020, and that dust was advected over the AERONET site from 18:00-20:30 UTC, we next turn our attention to the retrievals of τ from the CIMEL. Firstly, according to the CL51 profiles the atmosphere directly over the site was cloud-free until 20:40 UTC, when clouds at elevations of 3.2 to 4.9 km were detected (Fig. 2b). Consistent with the CL51 data, the 5-minute GOES-R imagery from 18:03-20:23 UTC shows that there were no clouds near the site during these times that could have been casting a shadow on CIMEL (Supplemental Data). As such, τ retrievals from the CIMEL measurements during this time span reflect the presence of aerosols in the atmospheric column and are not impacted by cloud contamination (hereafter τ is assumed to be at 500 nm unless otherwise specified).

On this day the L1 AERONET retrievals of 500 nm τ are near 0.05 at 18:00 UTC, which is just before dust is advected over the site, and then from 18:30 to 20:00 UTC the L1 τ increases to the maximum retrieved value of 0.57 (Fig. 3a, blue). Although τ is increasing during this time period, these measurements show increasing variance in dust concentrations over the site; between 19:30 and 20:00 UTC τ values increase from 0.25 to 0.47, drop down to 0.14, and then rise to 0.57. After the 20:00 UTC peak τ drops back to pre-outbreak values by 20:30 UTC. These τ data are consistent with the CL51 *BS* profiles, which show the largest *BS* values from 18:30 to 20:30 UTC, and a brief incidence of very low *BS* values just before the 20:00 UTC peak in τ (Fig. 2c).

The AERONET L1.5 τ retrievals (Fig. 3a, red) are in general only available when $\tau < 0.1$, meaning that the V3 algorithm has incorrectly identified the dusty measurements as cloud contaminated, effectively removing all of the optical depth retrievals during the dust outbreak from the L1.5 data record. We next identify the specific tests in the AERONET V3 algorithm (Table 1) that resulted in the rejection of τ retrievals during this dust outbreak.

a. Triplet Criterion

Each reported value of τ is based on three individual direct solar irradiance measurements made within a 1-minute interval (a so-called triplet measurement). If the variability of a triplet measurement made at the 675, 870, or 1020 nm wavelengths is greater than $0.015 \times \tau$ (retrieved at that wavelength) or 0.01, whichever is larger, than the measurement is rejected as possibly cloud contaminated. We applied this triplet variability threshold test to the L1 τ retrievals. Of the 28 retrievals of τ from the 18:30–20:30 UTC time period, 26 were rejected as cloud contaminated due to the triplet measurements exceeding these threshold values (Fig. 3b).

The highly variable nature of the *BS* profile during the dust outbreak (Fig. 2c) is qualitatively consistent with these high triplet variability values. For each AERONET observation we generated a set of CL51 "triplet" measurements by linearly interpolating the CL51 optical depth retrievals to the AERONET observation times, which we interpret as the reported triplet observation time, and then 30 s and 60 s past this time. The average of these three retrievals is an equivalent CL51 triplet optical depth at 910 nm $\tau_{cl,910}$ (Fig. 4a, horizontal axis values).

We next compare $\tau_{cl,910}$ to the AERONET 870 nm optical depth τ_{870}, since this is the closest AERONET wavelength to the ceilometer nominal wavelength of 910 nm, and since τ_{870} is one of the three wavelengths used in the triplet variability test (Table 1). An analysis of $\tau_{cl,910}$ and τ_{870} for the 18:00-21:00 UTC time period, which includes 40 data points, suggests that $\tau_{cl,910}$ is approximately proportional to τ_{870} (Fig. 4a), where the data are correlated at an r-value of 0.89 (p-value < 0.01). For the three retrievals where $\tau_{870} > 0.3$ (Fig. 2a, vertical axis) the CL51 proprietary algorithm did not retrieve extinction coefficients high enough into the atmospheric column (e.g., the top of the aerosol layer was incorrectly identified) and thus the CL51 optical depth retrievals underestimate the true optical depth at these times.

We estimate an 870 nm optical depth $\tau_{cl,870}$ from the CL51 data as

$$\tau_{cl,870} = c_1 \times \tau_{cl,910} + c_2 \tag{1}$$

where the constants c_1 and c_2 are determined via linear least squares regression of τ_{870} onto $\tau_{cl,910}$ using data collected during the time period 18:00-21:00 UTC, and which have values of 3.6×10^{-3} and 0.21, respectively (Fig. 4a, black dashed line). A comparison of the AERONET τ_{870} and the CL51 $\tau_{cl,870}$ suggests good agreement with a RMSE of 0.043 (Fig. 4b). We also estimated $\tau_{cl,870}$ by first using 1020-870 nm Angstrom exponent values from AERONET to generate an initial estimate of $\tau_{cl,870}$, and then using linear regression to “calibrate” the ceilometer optical depth to that from AERONET, obtaining qualitatively identical results.

We apply Eq. 1 to the individual CL51 “triplet” measurements in order to calculate an equivalent CL51 triplet variability at 870 nm, which is the difference between the maximum and minimum values for each triplet (Fig. 5). The correlation between the AERONET and the CL51 Triplet Variability estimates is statistically significant (r-value 0.60, p-value< 0.01) and the RMSE is 0.026. The agreement in the triplet variability from AERONET and the CL51 is not as good as that for τ (Fig. 4b), although this is not surprising since the CL51 retrievals of τ have a temporal resolution of 36 s but we are interpolating the measurements to 30 s intervals, and because we do not know the exact times of the AERONET triplet observations. We experimented with adjusting the timing of the CL51 “triplets” in order to generate a better fit to the AERONET data, but were not able to produce a better fit than that shown in Fig. 5. Nonetheless, the CL51 and AERONET 870 nm triplet variability estimates are consistent in that they both show that the triplet variability is greater than the threshold of 0.01 for most of the 37 data points between 18:00 and 21:00 UTC; from the AERONET data 30 of the 37 triplet variability estimates exceed the threshold of 0.01, and from the CL51 data 33 of these estimates exceed this threshold (Fig. 5). Thus, the CL51 measurements corroborate the high triplet variability seen during the 18:00-21:00 UTC time period, suggesting that these AERONET measurements are reflecting a physical signal in the dust and are not due to artifacts in the data collection process or cloud contamination.

b. Smoothness Check

Another step in the cloud screening procedure is to check the "smoothness" of the time series of τ. Specifically, if the rate of change of 500 nm τ between subsequent measurements is greater than 0.1 min^{-1}, then the larger of the two τ values is classified as cloud contaminated and removed. This procedure is then repeated until the rate of change of any two adjacent values of τ is below this threshold value for a given day. We applied this "smoothness" test to the L1 AERONET data, finding that it removed 11 of the 28 τ retrievals (Fig. 3c).

c. 3σ test

Within the V3 algorithm the 3σ test removes data points if τ at 500 nm is 3 standard deviations greater than the distribution mean for a given day. For the January 29 case the 3σ test only removed data points that were also removed by the Smoothness Check. Therefore, we do not provide a separate analysis for this component of the V3 algorithm beyond that which is done for the Smoothness Check.

d. Solar Aureole Curvature Check

At hourly increments the CIMEL instrument measures radiances L_A along the almucantar and principal planes, and the radiances measured at small scattering angles ψ with the sun are used to characterize the curvature of the forward scattering peak. Specifically, two metrics describing the curvature k_o and slope M of the forward scattering peak are calculated for each almucantar and principal plane scan. Firstly,

$$\ln L_A = a + b \ln \psi$$

is solved via linear least-square regression for each set of positive and negative scattering angles between 3.2° and 6°, for cases where the correlation coefficient between L_A and ψ for this subset of angles is greater than 0.99 (and for ψ in units of radians). Then these coefficients are used to describe the forward scattering peak slope

$$M = 1 - 2b$$

and curvature

$$k_o = \exp\left[-a(1-2b)\ln \psi_o\right]$$

where ψ_o is the smallest scattering angle in the 3.2° and 6° range (also in radians). Since ice particles are associated with a strong forward scattering peak, ice clouds are assumed to be present if $k_o < 2 \times 10^{-5}$. However, dust also typically exhibits a strong forward scatter peak (Ding et al. 2009), so an additional criteria of $M > 4.3$ is added to distinguish dust from thin cirrus. If these two thresholds are exceeded, then all measurements within 30 minutes of the almucantar or principal plane scan are classified as cloud contaminated.

We apply this Solar Aureole Curvature Check to the January 29 L1 data during the 18:00-21:00 UTC time period. We found that k_o and M from the almuncantar scan at 18:59 UTC exceeded these thresholds, which would have resulted in all of the L1 τ estimates from 18:30-19:30 UTC being rejected as cloud contaminated, corresponding to half of the 28 retrievals of τ made during the dust outbreak and when $\tau > 0.1$ (Fig 3d).

e. Reverse Spectral Dependence Test

Lastly, the L1 data undergo a decision tree algorithm that uses τ and angstrom exponents AE at various wavelengths to identify cloud contamination (Giles et al. 2019, their Fig 12). When the Reverse Spectral Dependence Test is applied to the L1 data on January 29 this test causes rejection of 17 of the 28 τ measurements during the peak of the dust outbreak from 18:30-20:30 UTC (Fig. 3e).

We identified the key components of the reverse spectral dependence test that resulted in the majority of these rejected retrievals of τ during the dust outbreak. Firstly, 12 measurements were rejected based on the following criteria,

$$AE_{440,870} < 0.2$$

$$\tau_{1020} > \tau_{675}$$

$$\tau_{1020} > \tau_{870}$$

$$AE_{870,1020} < 0$$

where the subscripts on AE indicate the wavelength pairs for which the exponent is calculated, and the subscripts on τ indicate the wavelength of the optical depth, both in nm units. In general, we find that as dust concentrations increase AE tends towards lower values, which is consistent with measurements made in North Africa (Toledano et al. 2009).

Next, we found that 11 of the measurements were rejected based on the criteria,

$$AE_{440,870} < 0.2$$

$$\tau_{1640} > \tau_{870}$$

$$\tau_{1640} > \tau_{1020}$$

$$AE_{870,1640} < 0$$

Similar to the previous case, as dust concentrations over the site grew *AE* tended toward lower values.

f. High AOD Restoration Test

We note that within the Version 3 algorithm there is a test intended to restore high values of τ that were rejected as cloud contaminated. The criteria for this check is that if $\tau_{500} > 0.5$ the measurement will be restored as not contaminated if,

$$AE_{675,1020} > 1.2$$

$$AE_{870,1020} > 1.3$$

There was one measurement on January 29 for which $\tau_{500} > 0.5$, where $\tau_{500} = 0.57$ at 19:58 UTC (Fig. 3). At this time $AE_{675,1020} = -0.05$ and $AE_{870,1020} = -0.04$, both well below the threshold for restoring the high optical depth retrieval. Furthermore, during the 18:30-20:30 time period the *AE* values for this restoring test are all near zero; the average $AE_{675,1020}$ during the dust outbreak is 0.01, and the average $AE_{870,1020}$ is 0.02. Such low values of the *AE* in the visible part of the spectrum is consistent with AERONET-based studies of the optical properties of dust (Tanré et al.

2001; Kim et al. 2011). Therefore, the restoring test is likely ineffective for periods of high dust concentrations at this AERONET site.

4. Discussion

In the previous section we documented that retrievals of τ during a dust outbreak on January 29 at an AERONET station near the Salton Sea were rejected as cloud contaminated and we identified the specific components of the V3 algorithm that led to the removal of those measurements. But how common is this for dust events at this site? While our own anecdotal evidence suggests that rejection of L1 retrievals of τ during dust outbreaks is pervasive, we attempted to quantify such effect by repeating our analysis of January 29, 2020 for 12 additional days during which there were dust outbreaks. We selected these days (Table 2) since for each, dust was clearly visible in satellite imagery, Roundshot camera images, and the ceilometer *BS* profiles, and there was not an obvious influence from other aerosol types (e.g., advection of smoke over the site). We identified continuous cloud-free time spans as those for which the ceilometer measurements indicated cloud-free conditions within 30 minutes of the Cimel measurement time, and from visual inspection of satellite imagery. This is not an exhaustive list of dusty and clear-sky conditions at this location.

The distribution of AERONET L1 τ is skewed with a long tail towards high τ; the median value of τ is 0.17 and the range is from 0.02 to 0.46 (Fig. 6a, blue). For these dust retrievals the cloud screening algorithm rejected 84% of the L1 retrievals as contaminated, and rejected 95% of the retrievals for $\tau > 0.1$ as being contaminated. Consequently, the distribution of L1.5 τ is quite different than that for the L1 data, with a median τ of 0.05 and a range of 0.02 to 0.18 (Fig. 6a, orange). Furthermore, the mean τ for the L1 retrievals (0.17) is more than a factor of two greater than that for the L1.5 retrievals (0.08).

We examined the roles of the Triplet Variability, Solar Aureole Curvature, and Reverse Spectral Dependence Tests (Table 1) in rejecting these dusty measurements since these three tests resulted in the largest rejection of data for the January 29, 2020 case, and since data removed by the Smoothness Check was mostly also removed by the Triplet Criterion. For these three tests we found that 60% of the rejected L1 retrievals failed the Triplet Criterion, meaning that the dust concentrations were highly variable in time. Indeed, most of the *BS* profiles for these days were qualitatively similar to that for January 29 (Fig. 2c), with rapidly changing periods of high and low dust concentrations (not shown). Approximately 16% of these measurements failed the Solar Aureole Curvature Check, reflective of the strong forward scattering peak of dust. Lastly, 27% of the measurements failed the Reverse Spectral Dependency Test, which mainly reflects the low values of the angstrom exponent for dust in the near infrared range.

While the high temporal variance of dust advected over the site appears to be the main reason for rejection of dusty retrievals of τ, on days for which the dust signal varies more smoothly in time the spectral signature of the dust aerosols still resulted in the rejection of data by the V3 algorithm. For example, on June 8 2020 there was a gradual buildup of dust over the site, which was corroborated by concurrent PM_{10} measurements (not shown), and during this time 20 of the 26 L1 τ retrievals failed the Reverse Spectral Dependency Test.

In order to recover these dusty AERONET measurements we developed a simple algorithm based on the CL51 measurements that will restore the rejected L1 retrievals of τ. This dust-restoration algorithm is only applied if the L1 $\tau > 0.1$, since the loss of dusty measurements is most pronounced when τ is greater than this value (Figs 3a, 6a), and if the L1.5 τ is not retrieved (i.e., the measurement has been flagged as contaminated). Available from AERONET are retrievals of the fine mode fraction f, which is an estimate of the fraction of particles with a diameter less than 10 μm (Dubovik et al. 2002). We identified 647 dusty measurements on the days in Table 2 for which $\tau > 0.1$ and the data were classified by the V3 algorithm as potentially cloud-contaminated. Of these measurements 97% of have values of $f < 0.5$ (Fig. 7), and thus we only apply this dust restoring algorithm for f below this value.

Our own analysis suggests that the criteria of L1 $\tau > 0.1$ and $f < 0.5$ will be met primarily for measurements of thin cirrus and dust. Thus, we assume the scene is cloud free if the CL51 has not reported a cloud within 30 minutes of the measurement time, which is a time span used to estimate fractional horizontal cloud cover from upward looking ceilometers (Wagner and Kleiss 2016). We noted cases where very thin and high clouds were not identified by the CL51 processing software. Thus, we applied the additional constraints that for a given day there should be more than 5 L1 retrievals of τ that meet the above criteria, since days with dust outbreaks typically loft dust over the site for more than 30 minutes. Furthermore, the L1 and CL51 retrievals of τ for each day must be positively and significantly correlated (p-value < 0.05). Since τ for the CL51 is only retrieved in the lower 4 km of the atmosphere, during dust outbreaks the retrievals of τ for both the AERONET and CL51 are typically positively and significantly correlated (e.g., Fig. 5a), whereas in the case of cirrus contamination, τ from the CL51 is not affected by these high clouds while τ from the AERONET instrument is. This dust restoring algorithm is summarized in Table 4.

When applied to the L1 data for the 12 days in Table 2 the algorithm described above restored 98% of the dusty τ retrievals for which the L1 $\tau > 0.1$ and $f < 0.5$ (Fig 6b). The L1.5 dust-restored τ nearly perfectly matches that for the L1 data (Fig. 6a) for $\tau > 0.1$; the median and range of the L1.5 dust-restored τ is 0.17 and 0.02 to 0.46, respectively. When applied to the Jan 29, 2020 case (Fig. 3a) the algorithm restored all of the measurements for which $\tau > 0.1$ and $f < 0.5$.

Examination of the CL51 cloud products suggests that the instrument's processing software occasionally fails to identify thin and high cirrus clouds. In order to test our algorithm for such cases we identified 32 days during which thin high cirrus were present over the region. For these days, we further identified four time spans during which thin high cirrus were present but the CL51 processing software failed to correctly detect the clouds (Table 3). There were 32 AERONET measurements falling within these time spans, which include 26 L1 retrievals where $\tau > 0.1$ and $f < 0.5$. For these data (and more broadly for those days) our algorithm did not restore any of the L1 measurements as being dusty, suggesting a false-positive rate of zero.

5. Conclusion

Here we presented measurements of dust made at a site in the far western Sonoran Desert and adjacent to the rapidly drying Salton Sea (Fig. 1). An analysis of AERONET retrievals of τ made at this site and during a dust storm on January 29, 2020 suggested that the AERONET V3 algorithm (Giles et al. 2019) misidentified dusty measurements as cloud contaminated, and thus rejected these data from inclusion in the AERONET L1.5 data set (Fig. 3a). Via an examination of satellite data, camera imagery, and backscatter profiles (Fig. 2) we were able to confirm that these observations were made during dusty and cloud free conditions.

One reason for the rejection of AERONET measurements on this day was the high temporal variability of τ (Fig. 3b). An analysis of τ retrieved from the ceilometer (Fig. 5) strongly suggested that this high temporal variability reflected the physical nature of the dust plumes over the area and was not due to any artifacts in the data collection or processing methodologies. We found that the strong forward scattering peak of dust resulted in the rejection of measurements via a check intended to identify thin cirrus (Fig. 3d). We also found that the relatively small variations in τ as a function of wavelength gave Angstrom Exponent values that were near-zero during the dust outbreak, thus also resulting in the rejection of measurements (Fig. 3e). As such, these dusty measurements failed several of the V3 cloud screening tests.

We repeated our analysis of the January 29 case for 12 other days during time periods when we were confident that there were otherwise clear-sky conditions (Table 2). Our results were consistent with the case study in that most of the measurements for $\tau > 0.1$ were rejected by the V3 algorithm (Fig 6), and that this loss of data resulted in more than a factor 2 reduction in τ averaged over these dusty time periods. Similar to the Jan 29 case dust was rejected due to: 1) high temporal variability, 2) low Angstrom Exponent values, and 3) strong forward scattering characteristics. We then described a simple algorithm to identify and restore dusty measurements that were incorrectly rejected as cloud contaminated by the V3 algorithm using collocated measurements from the CL51. When we applied this algorithm to the cases examined here we found that the algorithm restored nearly 100% of the dusty measurements for which $\tau > 0.1$ and $f < 0.5$.

This work illustrates the challenges of using sun photometery in a location close to several dust source regions, and suggests that supplemental collocated instrumentation may be needed to aid in the discrimination of dust and cirrus in places like the Salton Basin. The restoring algorithm described here cannot be scaled-up to other AERONET sites in dusty locations since it relies on collocated measurements from a ceilometer. Preliminary work exploring restoring algorithms that only utilize AERONET data showed promising results, although more work would be required to draw from a larger sample than just one AERONET site.

We note that during the first 4 months of 2021 the site frequently experienced issues related to dust contamination inside the collimator tubes, which resulted in an unphysical diurnal signal in the retrievals of τ that was apparent during more pristine-sky days, as discussed in Giles et al. (2019). This problem was ameliorated by more frequent cleaning of the filter windows and by blowing more compressed air through the detached tubes.

We are unaware of similar pervasive rejection of dusty scenes at other existing AERONET sites in desert regions, although preliminary work has suggested that similar effects may occur elsewhere (e.g., the Tamanrasset INM site on March 13 during the Terra and Aqua overpasses at 10:50 and 12:20 UTC). Closed topographic depressions like the Salton Basin are globally widespread, often contain highly erodible soil (Prospero et al. 2002; Mahowald et al. 2003; Engelstaedter et al. 2003), and may account for 30% of the global dust burden (Ginoux et al. 2012). Thus, it is at least plausible that regular misclassification of dusty measurements may have occurred–or will in the future occur–at other similarly located AERONET sites, particularly since the strong forward scattering peak and low Angstrom Exponent values are common features of mineral aerosols (Toledano et al. 2009; Ding et al. 2009). As such, this work can serve as a starting point for identifying and solving such challenges at other locations.

Acknowledgments. Funding for this work was provided by NSF Award AGS-1833173. The authors thank Brent Holben, David Giles, and the AERONET team at NASA Goddard Space Flight Center for helping with CIMEL sunphotometer installation and operations, for calibrating and maintaining the instrument, and for providing a detailed explanation of data screening/processing algorithms. The authors also thank two anonymous reviewers for their comments on a previous version of this manuscript. AERONET data is available at `aeronet.gsfc.nasa.gov`. MODIS imagery is from the NASA Worldview application `worldview.earthdata.nasa.gov`, part of the NASA Earth Observing System Data and Information System (EOSDIS). GOES-17 data was accessed via `class.noaa.gov`. Roundshot camera imagery is from `iid.roundshot.com`. Surface and upper air analysis were accessed from `www.wpc.ncep.noaa.gov` and archived Area Forecast Discussions from the San Diego National Weather Service field office was obtained at `mesonet.agron.iastate.edu`. Regional wind speed and direction and PM_{10} measurements are available from the California Air Resources Board `www.arb.ca.gov/aqmis2/aqdselect.php`. Site CL51 backscatter and extinction profiles are available upon request.

References

Albani, S., and Coauthors, 2014: Improved dust representation in the community atmosphere model. *Journal of Advances in Modeling Earth Systems*, **6 (3)**, 541–570.

Ansmann, A., and Coauthors, 2008: Influence of saharan dust on cloud glaciation in southern morocco during the saharan mineral dust experiment. *Journal of Geophysical Research: Atmospheres*, **113 (D4)**.

Das, R., A. Evan, and D. Lawrence, 2013: Contributions of long-distance dust transport to atmospheric p inputs in the yucatan peninsula. *Global Biogeochemical Cycles*, **27 (1)**, 167–175.

DeMott, P. J., and Coauthors, 2010: Predicting global atmospheric ice nuclei distributions and their impacts on climate. *Proceedings of the National Academy of Sciences*, **107 (25)**, 11 217–11 222.

Ding, S., Y. Xie, P. Yang, F. Weng, Q. Liu, B. Baum, and Y. Hu, 2009: Estimates of radiation over clouds and dust aerosols: Optimized number of terms in phase function expansion. *Journal of Quantitative Spectroscopy and Radiative Transfer*, **110 (13)**, 1190–1198.

Dubovik, O., B. Holben, T. F. Eck, A. Smirnov, Y. J. Kaufman, M. D. King, D. Tanré, and I. Slutsker, 2002: Variability of absorption and optical properties of key aerosol types observed in worldwide locations. *Journal of the atmospheric sciences*, **59 (3)**, 590–608.

Dubovik, O., and M. D. King, 2000: A flexible inversion algorithm for retrieval of aerosol optical properties from sun and sky radiance measurements. *Journal of Geophysical Research: Atmospheres*, **105 (D16)**, 20 673–20 696.

Dubovik, O., A. Smirnov, B. Holben, M. King, Y. Kaufman, T. Eck, and I. Slutsker, 2000: Accuracy assessments of aerosol optical properties retrieved from aerosol robotic network (aeronet) sun and sky radiance measurements. *Journal of Geophysical Research: Atmospheres*, **105 (D8)**, 9791–9806.

Engelstaedter, S., K. Kohfeld, I. Tegen, and S. Harrison, 2003: Controls of dust emissions by vegetation and topographic depressions: An evaluation using dust storm frequency data. *Geophysical Research Letters*, **30 (6)**.

Evan, A. T., 2019: Downslope winds and dust storms in the salton basin. *Monthly Weather Review*, **147 (7)**, 2387–2402.

Fernald, F. G., 1984: Analysis of atmospheric lidar observations: some comments. *Applied optics*, **23 (5)**, 652–653.

Giles, D. M., and Coauthors, 2019: Advancements in the aerosol robotic network (aeronet) version 3 database–automated near-real-time quality control algorithm with improved cloud screening for sun photometer aerosol optical depth (aod) measurements. *Atmospheric Measurement Techniques*, **12 (1)**, 169–209.

Ginoux, P., J. M. Prospero, T. E. Gill, N. C. Hsu, and M. Zhao, 2012: Global-scale attribution of anthropogenic and natural dust sources and their emission rates based on modis deep blue aerosol products. *Reviews of Geophysics*, **50 (3)**.

Habib, A., B. Chen, B. Khalid, S. Tan, H. Che, T. Mahmood, G. Shi, and M. T. Butt, 2019: Estimation and inter-comparison of dust aerosols based on modis, misr and aeronet retrievals over asian desert regions. *Journal of Environmental Sciences*, **76**, 154–166.

Holben, B. N., and Coauthors, 1998: Aeronet—a federated instrument network and data archive for aerosol characterization. *Remote sensing of environment*, **66 (1)**, 1–16.

Huneeus, N., and Coauthors, 2011: Global dust model intercomparison in aerocom phase i. *Atmospheric Chemistry and Physics*, **11 (15)**.

Jin, Y., and Coauthors, 2015: Ceilometer calibration for retrieval of aerosol optical properties. *Journal of Quantitative Spectroscopy and Radiative Transfer*, **153**, 49–56.

Kim, D., M. Chin, H. Yu, T. Eck, A. Sinyuk, A. Smirnov, and B. Holben, 2011: Dust optical properties over north africa and arabian peninsula derived from the aeronet dataset. *Atmospheric Chemistry and Physics*, **11 (20)**, 10 733–10 741.

Kok, J. F., and Coauthors, 2017: Smaller desert dust cooling effect estimated from analysis of dust size and abundance. *Nature Geoscience*.

Mahowald, N. M., R. G. Bryant, J. del Corral, and L. Steinberger, 2003: Ephemeral lakes and desert dust sources. *Geophysical Research Letters*, **30 (2)**.

Mahowald, N. M., and Coauthors, 2010: Observed 20th century desert dust variability: impact on climate and biogeochemistry. *Atmospheric Chemistry and Physics*, **10 (22)**, 10 875–10 893.

Marcos, C. R., J. L. Gómez-Amo, C. Peris, R. Pedrós, M. P. Utrillas, and J. A. Martínez-Lozano, 2018: Analysis of four years of ceilometer-derived aerosol backscatter profiles in a coastal site of the western mediterranean. *Atmospheric Research*, **213**, 331–345.

Miller, R., and I. Tegen, 1998: Climate response to soil dust aerosols. *Journal of climate*, **11 (12)**, 3247–3267.

Münkel, C., N. Eresmaa, J. Räsänen, and A. Karppinen, 2007: Retrieval of mixing height and dust concentration with lidar ceilometer. *Boundary-layer meteorology*, **124 (1)**, 117–128.

Myhre, G., and F. Stordal, 2001: Global sensitivity experiments of the radiative forcing due to mineral aerosols. *Journal of geophysical research*, **106 (D16)**, 18–193.

Okin, G. S., and Coauthors, 2011: Impacts of atmospheric nutrient deposition on marine productivity: Roles of nitrogen, phosphorus, and iron. *Global Biogeochemical Cycles*, **25 (2)**.

Peyridieu, S., and Coauthors, 2013: Characterisation of dust aerosols in the infrared from iasi and comparison with parasol, modis, misr, caliop, and aeronet observations. *Atmospheric Chemistry and Physics*, **13 (12)**, 6065–6082.

Prospero, J. M., P. Ginoux, O. Torres, S. E. Nicholson, and T. E. Gill, 2002: Environmental characterization of global sources of atmospheric soil dust identified with the nimbus 7 total ozone mapping spectrometer (toms) absorbing aerosol product. *Reviews of geophysics*, **40 (1)**.

Tanré, D., and Coauthors, 2001: Climatology of dust aerosol size distribution and optical properties derived from remotely sensed data in the solar spectrum. *Journal of Geophysical Research: Atmospheres*, **106 (D16)**, 18 205–18 217.

Toledano, C., V. Cachorro, A. De Frutos, M. Sorribas, N. Prats, and B. De la Morena, 2007: Inventory of african desert dust events over the southwestern iberian peninsula in 2000–2005 with an aeronet cimel sun photometer. *Journal of Geophysical Research: Atmospheres*, **112 (D21)**.

Toledano, C., M. Wiegner, M. Garhammer, M. Seefeldner, J. Gasteiger, D. Müller, and P. Koepke, 2009: Spectral aerosol optical depth characterization of desert dust during samum 2006. *Tellus B: Chemical and Physical Meteorology*, **61 (1)**, 216–228.

Wagner, T. J., and J. M. Kleiss, 2016: Error characteristics of ceilometer-based observations of cloud amount. *Journal of Atmospheric and Oceanic Technology*, **33 (7)**, 1557–1567.

Wiegner, M., and Coauthors, 2014: What is the benefit of ceilometers for aerosol remote sensing? an answer from earlinet. *Atmospheric Measurement Techniques*, **7 (7)**, 1979–1997.

Yang, S., J. Preißler, M. Wiegner, S. von Löwis, G. N. Petersen, M. M. Parks, and D. C. Finger, 2020: Monitoring dust events using doppler lidar and ceilometer in iceland. *Atmosphere*, **11 (12)**, 1294.

Zhou, Y., R. C. Levy, L. A. Remer, S. Mattoo, Y. Shi, and C. Wang, 2020: Dust aerosol retrieval over the oceans with the modis/viirs dark-target algorithm: 1. dust detection. *Earth and Space Science*, **7 (10)**, e2020EA001 221.

LIST OF TABLES

TABLE 1. AERONET Version 3 cloud screening tests most relevant to dusty conditions.

Test	Criteria for rejecting measurements
Triplet Criterion	Range of triplet retrievals of τ at 675, 870 & 1020 nm wavelengths $>$ Maximum of 0.01 or $0.015\times\tau$.
Smoothness Check	If $\Delta\tau/\Delta t > 0.1$ min^{-1}, for τ at 500 nm, reject the larger τ in the pair, then repeat.
Solar Aureole Curvature Check	1020 nm radiance measurements for scattering angles between 3.2° and 6° are used to determine forward scattering peak curvature k_o and slope M. If $k_o > 2\times10^{-5}$ & $M > 4.3$, τ retrievals within ±30 min of the radiance measurement are removed.
Reverse Spectral Dependence Test	Decision Tree algorithm consisting of various spectral threshold tests for AE and τ at 440, 675, 870, and 1020 nm wavelengths (Giles et al. 2019, Fig 12).

TABLE 2. AERONET measurement dates and start and stop times (UTC) identified as dusty and clear sky conditions.

Date	Start time	End time
09-Jan-2020	20:30	21:30
04-Feb-2020	16:50	18:15
01-Mar-2020	18:12	19:45
23-Mar-2020	17:25	18:35
06-Apr-2020	00:50	01:23
08-Jun-2020	14:34	16:28
25-Oct-2020	20:37	22:00
26-Oct-2020	20:37	21:37
12-Dec-2020	21:20	12:25
09-Mar-2021	20:10	21:55
15-Mar-2021	23:02	23:50
21-Apr-2021	21:10	22:43

TABLE 3. Dates and start and stop times (UTC) during which cirrus clouds are present but not identified by the CL51 processing software.

Date	Start time	End time
14-Jan-2020	22:40	23:33
28-Mar-2020	22:10	23:21
24-Oct-2020	17:51	18:07
07-Jan-2021	21:20	21:26

TABLE 4. Tests for the dust restoring algorithm for the Salton Sea AERONET site.

Dust restoring algorithm
$\tau > 0.1$ & $f < 0.5$ & No cloud detected ±30 min
If above conditions are met for 5 or more measurements during a given day:
r-value > 0 & p-value < 0.05 for those τ_{870} & $\tau_{cl,870}$ retrievals

LIST OF FIGURES

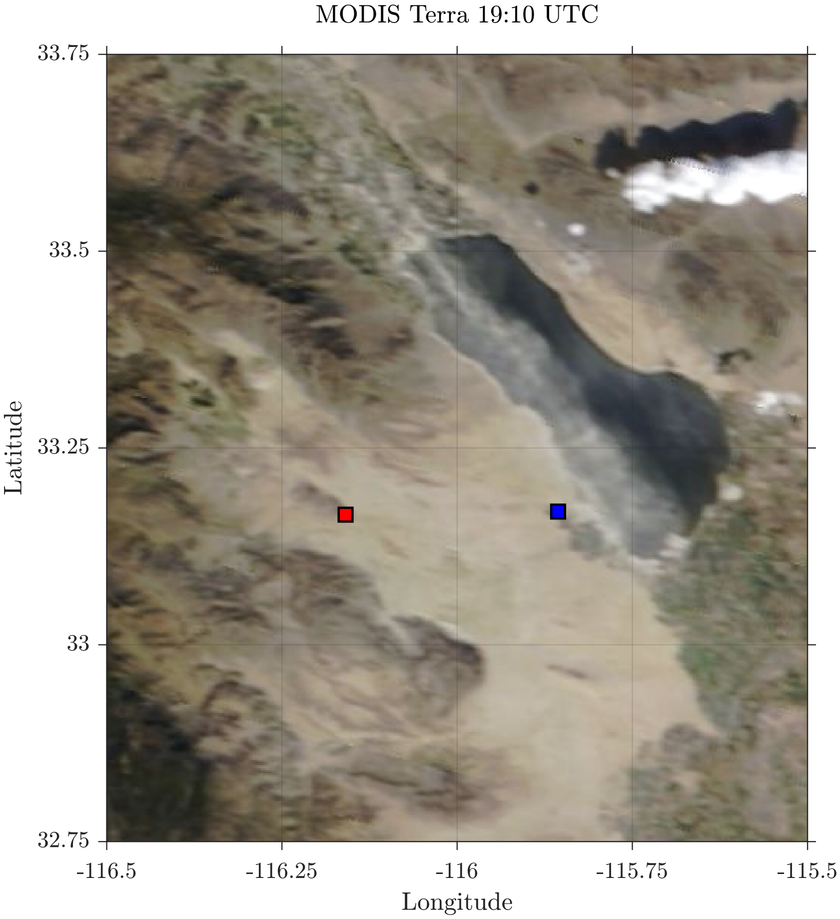

FIG. 1. Satellite image of a dust outbreak within the region of interest. Shown is a MODIS-Terra RGB image of a dust storm on January 29, 2020 at 20:10 UTC. The location of the Salton Sea AERONET site is indicated by the blue square, and the location of the 360° Roundshot Camera is indicated by the red square. The body of water is the Salton Sea. Although dust is present over much of the region, these mineral aerosols are most visible over the Salton Sea due to the contrast they make with the dark water surface.

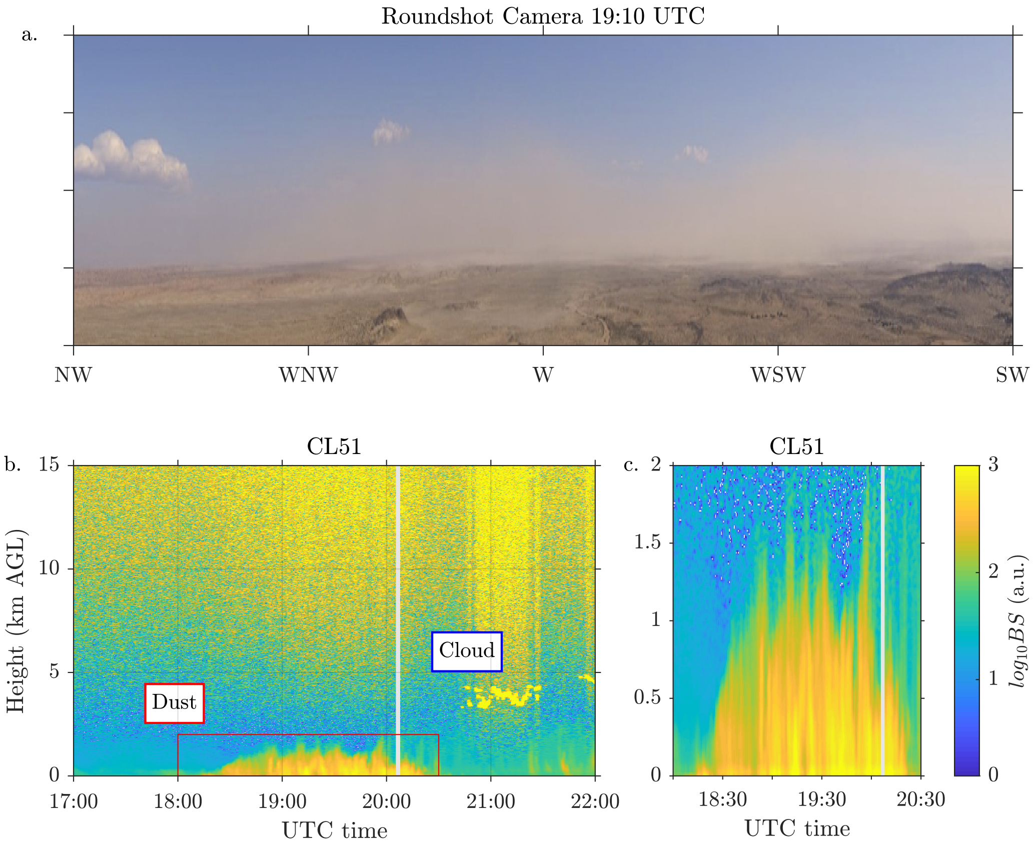

Fig. 2. Ceilometer and Roundshot imagery of the January 29, 2020 dust outbreak. In 2a is a Roundshot image acquired at 19:10 UTC, which corresponds to the time of the Terra overpass in Fig 1, and which shows dust west of the camera location (Fig 1). In 2b is a plot of the CL51 backscatter *BS* profile from 17:00-22:00 UTC. The main dust outbreak is highlighted by the red box, and cloud are indicated by high *BS* values just below 5 km below ground level starting just before 21:00 UTC. In 2c is a close-up of the *BS* profiles during the dust outbreak (red box in 2a).

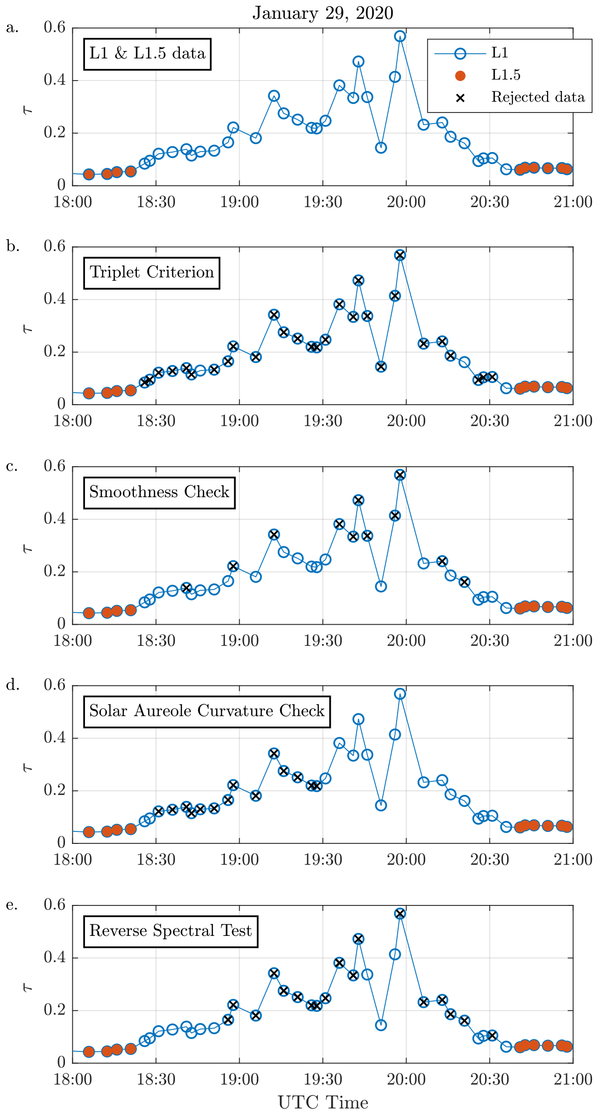

FIG. 3. Aerosol Optical depth retrievals on January 29, 2020. In 3a is a time series of τ at 500 nm from the AERONET L1 (blue circles) and cloud-screened L1.5 (red filled circles) retrievals. Clear-sky conditions persisted until just after 21:00 UTC, and so the lack of L1.5 retrievals from approximately 18:30 to 20:30 UTC indicate that the V3 algorithm misidentified the dust signal as cloud contamination. In 3b–e are the same L1 and L1.5 retrievals of τ, but where a black "x" indicates when a specific algorithm test triggered a rejection of the data.

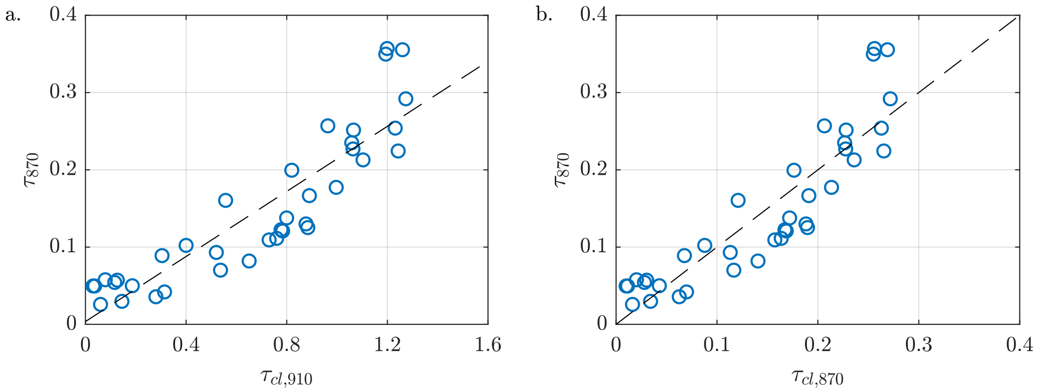

FIG. 4. Comparison of τ from AERONET and the CL51. Plotted in 4a are AERONET τ_{870} retrievals on January 29, 2020 from 18:00 to 21:00 UTC (vertical axis) and an estimate for these same times generated from extinction profiles retrieved from the CL51 *BS* data ($\tau_{cl,910}$, horizontal axis). In Fig 4b are the same AERONET τ_{870} retrievals, but plotted as a function of the estimated CL51 870 nm τ via Eq. 1 ($\tau_{cl,870}$, horizontal axis).

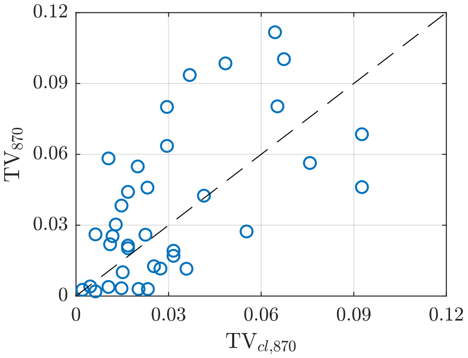

FIG. 5. AERONET and CL51 triplet variability comparison. Plotted are the 870 nm triplet variability TV estimates from AERONET (vertical axis) and CL51 (horizontal axis) at 870 nm. The dashed black line represents equivalence between the data sets and is used only for reference.

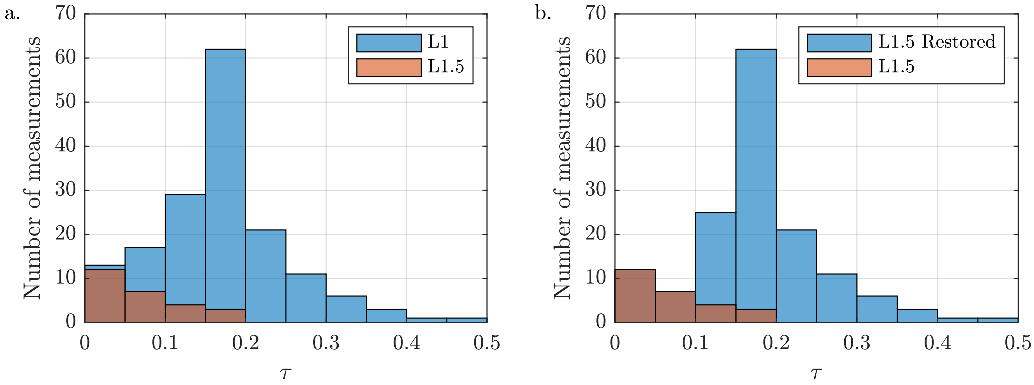

FIG. 6. Histograms of τ retrievals during dust storms on 12 days (Table 2). Shown in 6a are histograms of the L1 and L1.5 τ for the time spans indicated in Table 2. Shown in 6b is the histogram of the L1.5 τ after the application of a dust restoring algorithm. For reference the histogram of the L1.5 τ is also shown in 6b.

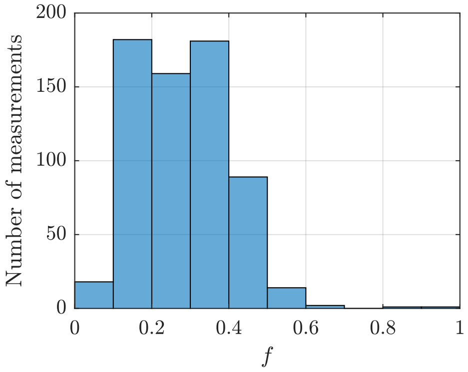

FIG. 7. AERONET fine mode fraction f retrievals during dust storms. Plotted is a histogram of f retrievals made during times with overhead dust and $\tau > 0.1$ during the 12 days in Table 2.